Three-micrometer-diameter needle electrode with an amplifier for extracellular in vivo recordings

Yuto Kita[a], Shuhei Tsuruhara[a], Hiroshi Kubo[a], Koji Yamashita[a], Yu Seikoba[a], Shinnosuke Idogawa[a], Hirohito Sawahata[a,b], Shota Yamagiwa[a], Xian Long Angela Leong[a], Rika Numano[c], Kowa Koida[d,e], and Takeshi Kawano[a,1]

[a]Department of Electrical and Electric Information Engineering, Toyohashi University of Technology, 1-1 Hibarigaoka Tempaku-cho, 441-8580 Toyohashi, Japan; [b]National Institute of Technology, Ibaraki College, 866 Nakane, 312-8508 Hitachinaka, Japan; [c]Department of Applied Chemistry and Life Science, Toyohashi University of Technology, 1-1 Hibarigaoka Tempaku-cho, 441-8580 Toyohashi, Japan; [d]Department of Computer Science and Engineering, Toyohashi University of Technology, 1-1 Hibarigaoka Tempaku-cho, 441-8580 Toyohashi, Japan; and [e]Electronics-Inspired Interdisciplinary Research Institute, Toyohashi University of Technology, 1-1 Hibarigaoka Tempaku-cho, 441-8580 Toyohashi, Japan

Edited by John A. Rogers, Northwestern University, Evanston, IL, and approved February 1, 2021 (received for review April 28, 2020)

Microscale needle-electrode devices offer neuronal signal recording capability in brain tissue; however, using needles of smaller geometry to minimize tissue damage causes degradation of electrical properties, including high electrical impedance and low signal-to-noise ratio (SNR) recording. We overcome these limitations using a device assembly technique that uses a single needle-topped amplifier package, called STACK, within a device of ∼1 × 1 mm^2. Based on silicon (Si) growth technology, a <3-μm-tip-diameter, 400-μm-length needle electrode was fabricated on a Si block as the module. The high electrical impedance characteristics of the needle electrode were improved by stacking it on the other module of the amplifier. The STACK device exhibited a voltage gain of >0.98 (−0.175 dB), enabling recording of the local field potential and action potentials from the mouse brain in vivo with an improved SNR of 6.2. Additionally, the device allowed us to use a Bluetooth module to demonstrate wireless recording of these neuronal signals; the chronic experiment was also conducted using STACK-implanted mice.

neural recording | microelectrode | MOSFET

Microscale needle-electrode devices, which allow brain tissue to be penetrated and electrical signals of neurons and cells to be recorded, have been a powerful means of understanding how the brain forms complete circuits, making significant contributions to neuroscience. Micro- and nanoscale fabrication technologies offer miniaturization of the needle-electrode geometry. The two-dimensional fabrication process produces a shank type of ∼40-μm-width needle electrode, called a "Michigan probe" (1, 2). This type of electrode is followed by a complementary metal–oxide–semiconductor (CMOS) amplifier array on each shank (3, 4). A wafer-dicing–based fabrication process produces the other type, a three-dimensional ∼80-μm -diameter needle array, called the "Utah array" (5, 6), which demonstrates the brain–machine interface (7, 8). However, these fabrication technologies face the issue of further miniaturization of the needle geometry, which is an important property of the electrode in terms of biocompatibility and application to chronic device implantation (9).

Saxena et al. reported that a 50-μm-thick Michigan probe enhanced the blood–brain barrier breach in electrode-implanted rats (10). Although the size of the needle is < 50 μm, an object with a dimension >20 μm is still subject to disruption of the local communication between glia, releasing proinflammatory cytokines and recruiting additional activated microglia and reactivated astrocytes (11–13). However, further needle geometry reduction to <10 μm leads to no major traumatic injury in the tissue (14).

On the basis of these findings, an "ultrasmall" needle electrode with a <10-μm diameter is necessary as the next step toward minimally invasive neuronal recording of the brain. A needle electrode with a diameter of ∼8.6 μm was fabricated using 7-μm-diameter carbon fibers and additional coating processes, demonstrating reduced chronic reactive tissue responses while a single neuron is recorded (15). A further small-needle electrode was produced by a silicon (Si) growth technology (gold-catalyzed vapor–liquid–solid [VLS] growth), resulting in needle-electrode diameters of ∼7 μm (16, 17) and ∼5 μm (18).

Needle-electrode miniaturization degrades the electrical property of signal-to-noise ratio (SNR) in the neuronal recording. Fig. 1*A* shows the fabrication process of the <10-μm-diameter needle electrode using an ∼1-μm-diameter Si needle and subsequent coatings of metal and insulating layers (e.g., platinum [Pt] and parylene). This electrode technology allows the needle to be reduced to <3 μm in diameter (18, 19). However, the electrolyte/metal interfacial electrical impedance of the electrode increased with a decrease in the area of the recording site of the metal, attenuating the amplitude of neuronal signals (17, 20) and degrading the SNR of the recording (Fig. 1 *B*, *I*). Although the electrode's impedance can be reduced using a low-impedance material [e.g., platinum black (Pt black) (21), iridium oxide, and poly(3,4-ethylenedioxythiophene) (PEDOT) (22)], this low-impedance material must be deposited on the needle, increasing the size (diameter) of the needle itself and limiting the needle miniaturization. Further, the reduction of the electrode's

Significance

Electrophysiology using microelectrodes has been used for understanding brain circuits, thereby making significant contributions to neuroscience. These electrodes should be miniaturized to <10 μm to reduce tissue damage; however, the small geometry of the electrodes causes degradation of the electrical properties. We overcome these limitations by using an assembly technique in which a <3-μm-diameter needle electrode with a length of 400 μm is stacked on an amplifier module. The needle electrode shows high electrical impedance and low signal-to-noise ratio in recordings; however, stacking the amplifier on the electrode improves these properties, as demonstrated by a neuronal recording using mice. Additionally, the device allows wireless recording via a Bluetooth module and implantation for chronic experiments.

Author contributions: T.K. designed research; Y.K., S.T., H.K., K.Y., Y.S., S.I., H.S., S.Y., and X.L.A.L. performed research; Y.K., S.T., H.K., K.Y., Y.S., H.S., R.N., K.K., and T.K. analyzed data; Y.K., S.T., K.Y., Y.S., H.S., and T.K. wrote the paper; and T.K. supervised the project.

The authors declare no competing interest.

This article is a PNAS Direct Submission.

Published under the PNAS license.

[1]To whom correspondence may be addressed. Email: kawano@ee.tut.ac.jp.

This article contains supporting information online at https://www.pnas.org/lookup/suppl/doi:10.1073/pnas.2008233118/-/DCSupplemental.

Published April 12, 2021.

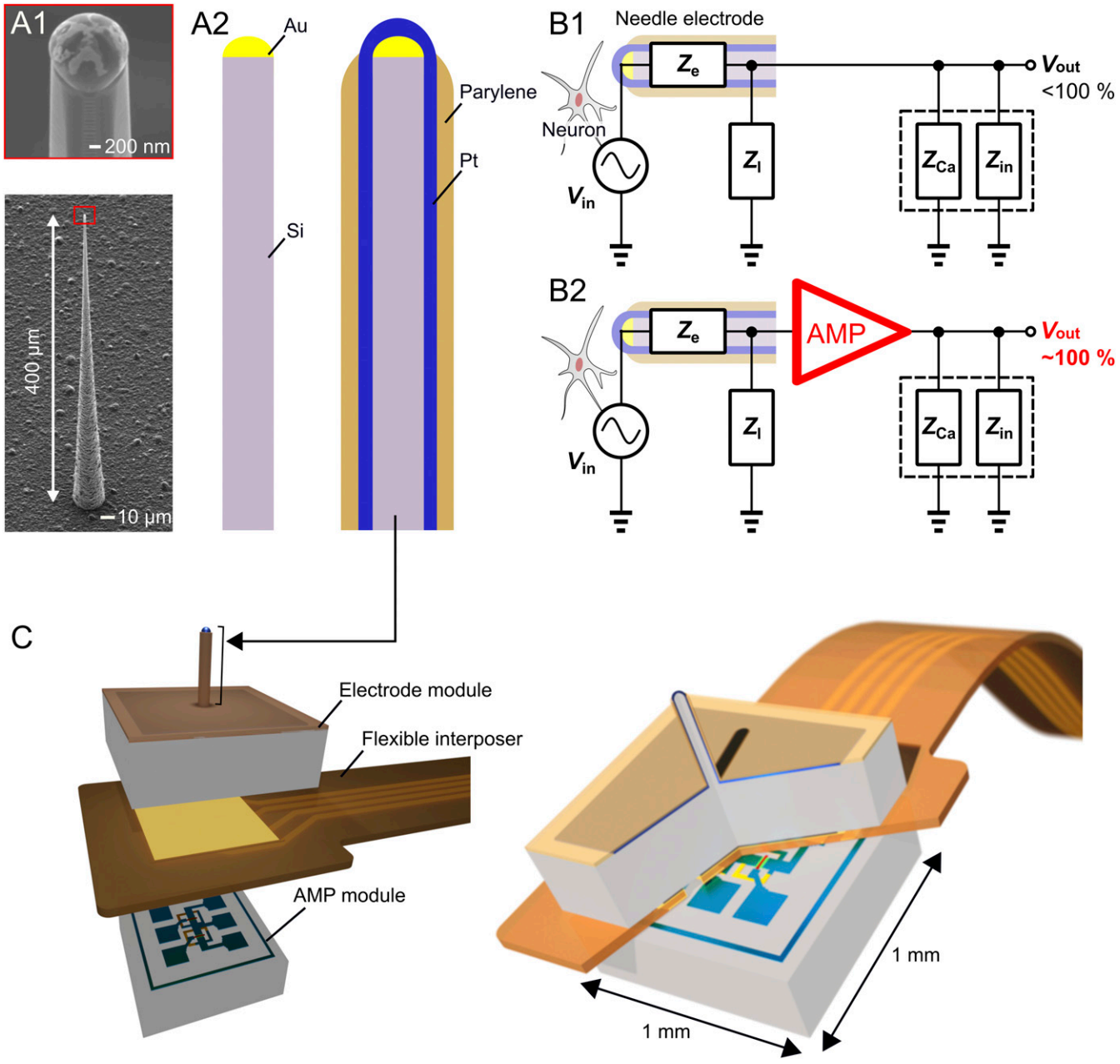

Fig. 1. A 3-μm-diameter needle electrode with an amplifier for extracellular recordings. (*A*) SEM images of an ∼1-μm-diameter Si needle by Si growth technology (*A*, *1*) and schematics of electrode fabrication (*A*, *2*). (*B*, *1*) Equivalent circuit model of the needle electrode in the neuronal recording. The recording system between the electrode and the recording amplifier consists of the needle's electrolyte/metal interfacial electrical impedance, Z_e, and parasitic impedances of device interconnection, Z_l, cable capacitance, Z_{Ca} and input impedance of the amplifier, Z_{in}. (*B*, *2*) Equivalent circuit model of the needle electrode with a head-stage AMP to improve electrical properties in the neuronal recording. (*C*) Schematics of the assembly technique of the STACK device, in which a module of the microneedle electrode is stacked on the other AMP module with a flexible interposer between them.

impedance is limited by both the area of the needle tip and the impedance of the deposited material.

Another method of improving the electrical properties of such an ultrasmall-needle electrode is to design a signal-buffering amplifier at the head stage of the electrode device (Fig. 1 *B*, *2* and *SI Appendix*, Text ST1 and Fig. S1). We demonstrated the on-chip integration of a metal–oxide–semiconductor field-effect transistor (MOSFET) amplifier with these needle electrodes, assembled by the post-MOSFET process of the VLS growth of the Si microneedle, using either the (111)-Si substrate (23, 24) or a hybrid substrate of (100)-top-Si/buried oxide/(111)-handle-Si (25, 26). However, both the needle and the amplifier were designed to be on the same surface side of the chip. Hence, the device had a relatively large area [e.g., 8×3 mm^2 for the surface-sided device interconnections (17, 18)], which had to be miniaturized to reduce the removal area of the cranium, particularly for a small brain (such as that of mice).

We propose an assembly technique in which a module of a <3-μm-tip-diameter microneedle electrode is stacked on another amplifier module, called the single needle-topped amplifier package (STACK) device, to overcome issues related to the electrical properties of an ultrasmall needle electrode of less

than 10 μm in diameter and the device area (Fig. 1*C*). We designed the device to be within ∼1 × 1 mm^2 for in vivo recording of neuronal activities in the mouse brain.

Method and Fabrication

Electrode Module. We used an electrode module with a 1 × 1-mm^2 size that comprised a 400-μm-length microneedle electrode at the center portion of a substrate of conductive Si [n-type (111)-Si, resistivity = <0.02 Ω cm, thickness = 525 μm] (18, 19) (Fig. 2 *A*, *1*). The Si microneedle was formed by the Au-catalyzed VLS growth of Si (27). A needle length of 400 μm was produced in a growth time of 6 h at ∼730 °C. The VLS-grown Si microneedle was metalized with a Pt layer and a titanium (Ti) binder (total Pt/Ti thickness = 200 nm). The Pt-coated Si needle was insulated with a highly biocompatible material of parylene-C (1 μm thick), except for the needle-tip section of Pt (Fig. 2 *A*, *2*). The electrolyte (saline)/metal (Pt) interfacial impedance of the needle measured in saline showed 5 ± 1 MΩ at 1 kHz (Fig. 2 *A*, *3*). Such high impedance of the electrode attenuates the amplitude of the neuronal signals in recordings because of the parasitic impedance between the device and the recording system (1 to 10 MΩ) (17, 20, 28).

Amplifier Module. We solved the issue of amplitude attenuation caused by the electrode's high impedance by using the other module of the amplifier (the "AMP module"). The AMP module played a role in the head stage in in vivo neuronal recordings. The AMP module is the same size of 1 × 1 mm^2 with a thickness of 525 μm, comprising a source follower circuit of the Si-MOSFET (Fig. 2 *B*, *1*). The source follower was fabricated by aluminum (Al)-interconnection-based in-house 5-μm-gate-length n-type MOSFET (NMOS) technology (25, 26). Fig. 2 *B*, *2* and *3* depicts the drain current I_D–gate voltage V_G characteristics and I_D–drain voltage V_D characteristics of an enhancement NMOS (gate width = 50 μm, gate length = 10 μm), respectively, fabricated through this technology. For the source follower, we designed the drive and load MOSFETs with the same gate dimensions of width *W*/length *L* = 50/10 μm. The source follower had a high input impedance of 460 MΩ at 1 kHz and an output impedance of 7.4 kΩ (1/transconductance, *SI Appendix*, Text ST1 and Fig. S1*B*), while the microneedle electrode impedance was ∼5 MΩ at 1 kHz (Fig. 2 *A*, *3*). Each MOSFET was designed in a separated p well. These p wells of load and drive MOSFETs were tied to V_{ss} and V_{out}, respectively, resulting in the elimination of the body effect of the drive MOSFET. Fig. 2 *B*, *4* shows the input–output voltage characteristics of the fabricated NMOS source follower. The voltage gain of the fabricated source follower was 0.98 (−0.175 dB), consistent with the theoretical value.

Device Assembly. The electrode and AMP modules were assembled in the same package by sandwiching an interposer between them. For the interposer, which also acted as the flexible cable between these modules and the recording system, we used a polyimide-based flexible printed circuit (FPC, 100 μm thick, *SI Appendix*, Fig. S2). First, the AMP module was mounted at the bottom of the interposer by flip-chip bonding (model 1300, HiSOL, Inc.) with an anisotropic conductive paste (ACP) at a bonding pressure of 15 N and a temperature of 150 °C. Another electrode module was mounted on top of the interposer with a conductive epoxy (CW2400, CircuitWorks) (*SI Appendix*, Fig. S3). Fig. 3 *A* and *B* shows the two assembled modules with the interposer. ACP played a role in the electrical connection between the bonding pads of the AMP module and the interposer, with an ohmic contact of ∼1.5 Ω (*SI Appendix*, Fig. S4). The overall thickness of the assembled device was ∼1 mm. Both the modules (i.e., electrode and AMP) of Si, except for the needle portion in the electrode module, were encapsulated with insulating ultraviolet curable resin because of the device's application to a saline environment in an in vivo recording (*SI Appendix*, Fig. S5).

Results

Electrical Properties. The output/input (O/I) signal-amplitude ratios of the fabricated STACK device were measured in saline by applying test signals at frequencies of 1 Hz to 10 kHz, in which the frequencies represented extracellular signals [a local field potential (LFP) of <100 Hz (29, 30) and an action potential (or spike) of ∼1 kHz] (Fig. 3*C*). The device voltage gain at the frequency range was >0.98 (−0.175 dB), which agreed with the theoretical gain as discussed in *Method and Fabrication*. For comparison, the graph also included the O/I ratio of the same electrode module without the stacking AMP module, demonstrating a decrease in the gain at 10 Hz and over [0.62 gain (−4.15 dB) at 1 kHz]. This decrease in gain was caused by the high-impedance characteristics of the needle electrode (5 ± 1 MΩ at 1 kHz) (Fig. 2 *A*, *3*) (17, 18, 20).

Fig. 3*D* shows the measured input-referred voltage noise spectrum for both needle electrodes, with and without the AMP module. The graph also includes instrumentation noise. The curve of the needle electrode with AMP presents a 1/*f* noise. All the noise curves peaked at a consistent frequency of ∼1 kHz because of the recording system used (*Materials and Methods*), and this should be eliminated in future recordings. The rms noise voltage of the needle electrode with the AMP module, which was taken from the output voltage waveforms, was 15.3 μV rms at 500 to 3,000 Hz (filtered for the frequency range of the action potential recording). Considering the rms noise and the signal of the 100-μV sine wave (1 kHz) as the neuronal activity, the AMP stacked needle electrode yielded an SNR of 4.52 (13.1 dB), which is higher than that without the AMP module [SNR = 2.96 (9.43 dB)].

In Vivo Recording. We demonstrated the neuronal recording capability of the fabricated STACK device using a mouse cerebral cortex in vivo (Fig. 4). The mouse (male, 26.8 g in weight) was anesthetized with an intraperitoneal injection using chlorprothixene (100 μL of 0.5% solution per 10 g body weight) and urethane (50 μL of 10% solution per 10 g body weight). After parts of the cranium and dura mater (0 to 2 mm caudal and 2 to 4 mm lateral to the bregma) were surgically removed, the device was placed on the barrel field in the primary somatosensory cortex (S1B), and the needle electrode subsequently penetrated the tissue with a needle depth of 400 μm (Fig. 4 *A* and *B*). The mouse's whiskers were physically stimulated during the recording to characterize the evoked neuronal potentials (*Materials and Methods*). The penetrated needle was connected to output lead pads both with and without the AMP module in the same FPC package; signals recorded via the same needle electrode were compared (with and without AMP).

Fig. 4 *C*, *1* shows the average waveform of low-frequency band signals (filtering = 1 to 300 Hz, *n* = 24 trials) derived from the S1B of the mouse via the needle electrode without AMP. The signals were in response to the whisker stimuli with a latency of ∼20 ms at the onset of the somatosensory evoked potential. The low-frequency band signal waveforms recorded via the same needle electrode with AMP (Fig. 4 *D*, *1*) were also in response to the whisker stimuli for a duration of ∼20 ms while showing peak-to-peak amplitudes of ∼350 μV. These signals recorded via the needle electrode both with and without the AMP module were evoked LFPs by whisker stimulation because of the waveforms and latency.

The high-frequency band signals (filtering = 500 to 3,000 Hz) taken from the same recording session were also characterized. Fig. 4 *C*, *2* shows the typical high-frequency band signal recorded via the needle electrode without the AMP module. Fig. 4 *C*, *3* and *4* depicts the raster plot diagrams and the peristimulus time

ENGINEERING

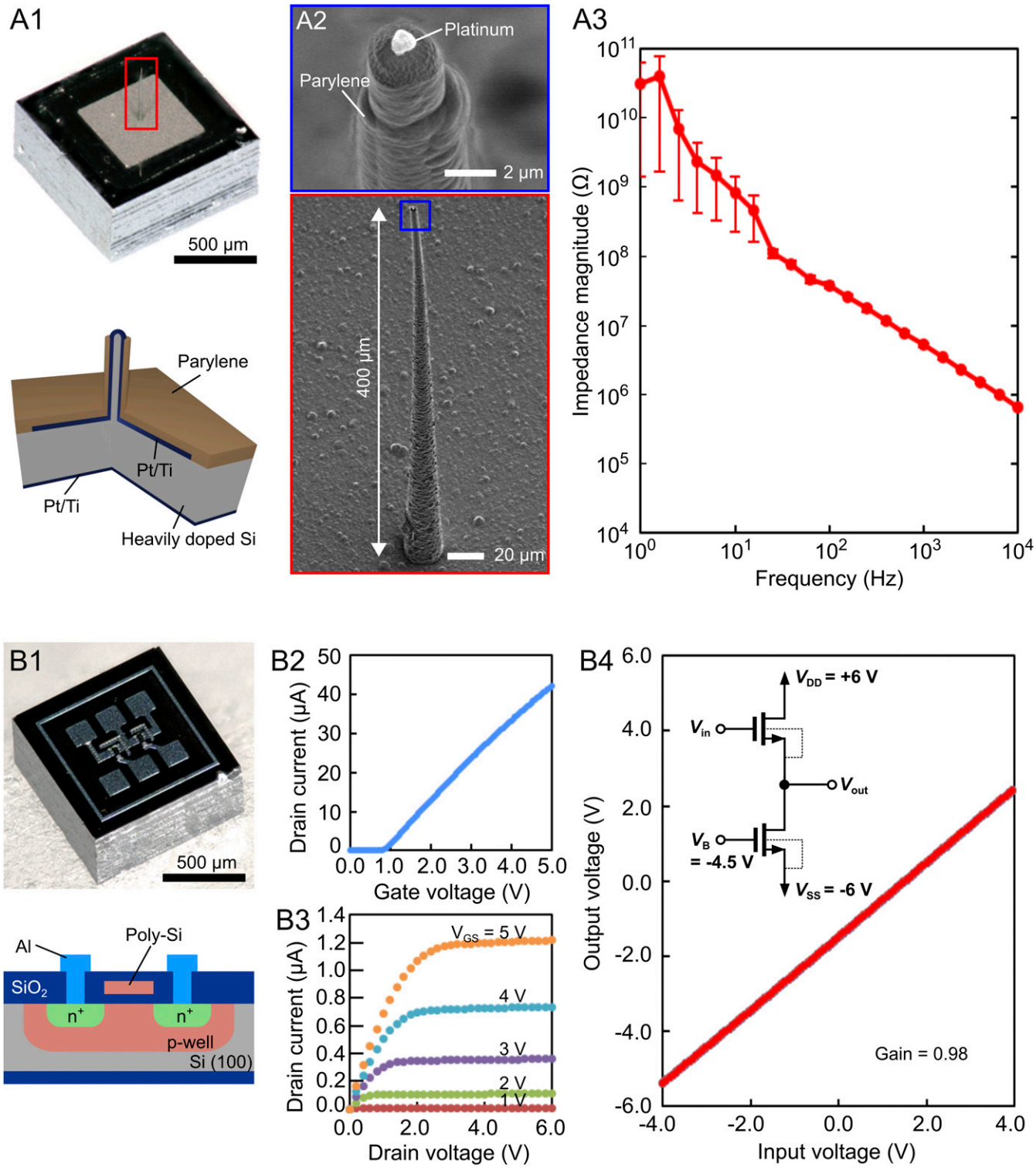

Fig. 2. Fabricated device modules. (*A*, *1–3*) Electrode module. (*A*, *1*) Photograph and cross-sectional schematic of the electrode module. The module has an area of 1×1 mm^2 with a microneedle electrode at the center portion. The substrate thickness is 525 μm. (*A*, *2*) SEM images of the <3-μm-diameter, 400-μm-length needle electrode. (*A*, *3*) Electrolyte (saline)/metal (Pt) interfacial impedance of the needle electrode measured in saline. (*B*, *1–4*) AMP module. (*B*, *1*) Photograph and cross-sectional schematic of the AMP module. The schematic represents the individual NMOS. (*B*, *2* and *3*) Drain current I_D–gate voltage V_G characteristics (*B*, *2*) and I_D–drain voltage V_D characteristics (*B*, *3*) of an enhancement NMOS (gate width = 50 μm, gate length = 10 μm). (*B*, *4*) Input voltage–output voltage characteristics of the fabricated NMOS source follower with a voltage gain of 0.98 (– 0.175 dB).

histograms (PSTHs), respectively, of these signals recorded without the AMP module, showing insignificant responses to the whisker stimuli. The detection thresholds of these signals were 3× the SD (σ) of the mean signal −0.5 to −1.0 s before the stimulus onset. However, the signals derived via the needle electrode with the AMP module comprised high-frequency band signals, which

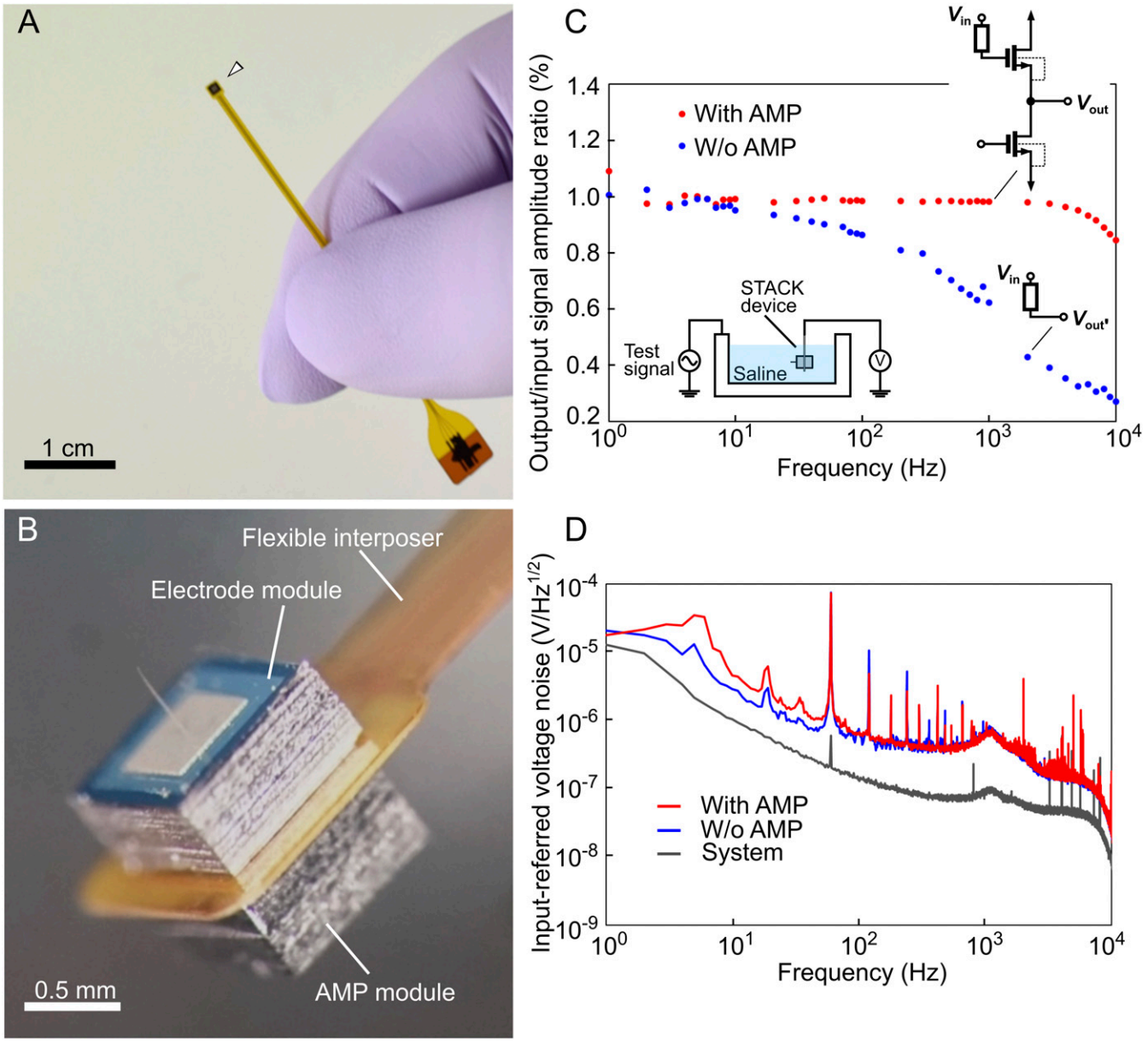

Fig. 3. Assembled STACK device. (*A* and *B*) Photographs of the assembled STACK device, in which the flexible interposer is sandwiched between the electrode and the AMP modules. The total device thickness, excluding the needle portion, is ∼1 mm (thicknesses: needle module = 525 μm, FPC = 100 μm, and AMP module = 525 μm). The sidewalls of each module (Si) are insulated with resin (*SI Appendix*, Fig. S5). (*C*) O/I signal amplitude ratios of the two types of needle electrodes with (red, with AMP) and without (blue, without AMP) the AMP module immersed in saline. Test signals of 150-μV peak-to-peak sinusoidal waves from 1 to 10,000 Hz are applied to the saline. These data with and without the AMP module are taken from the same needle electrode by assembling the needle electrode with and without the AMP module in the same FPC (flexible interposer) package. (*D*) Measured input-referred voltage noise spectrum for both needle electrodes with and without the AMP module.

were in response to the stimuli with the 20-ms duration. Fig. 4 *D*, *2* shows a typical high-frequency band-signal waveform comprising negative and subsequent positive amplitude peaks ranging from −23 to 15 μV (*SI Appendix*, Fig. S6*A*), similar to the waveform of extracellular action potentials recorded with a conventional tungsten microelectrode and a Pt-black–deposited >5-μm-diameter needle electrode (17, 18). Fig. 4 *D*, *3* and *4* shows the raster plot diagrams and the PSTHs, respectively, of these spikes recorded with the AMP module, using an amplitude threshold (3σ of the mean signal −0.5 to −1.0 s before stimulus onset, similar definition to Fig. 4 *C*, *3* and *4*). The firing peak appeared at ∼20 ms after stimulus onset, which was consistent with the latency of neuronal signals recorded with conventional microelectrodes. These results suggest that these spikes were evoked by the whisker stimuli. We also confirmed that these signals disappeared with pharmacological blocking with lidocaine (*SI Appendix*, Text ST2 and Fig. S7). These results suggest that the signals recorded via the STACK device represented neuronal activity.

Spike signals detected via the needle electrode with the AMP module were analyzed. Fig. 4 *E*, *1* shows enlarged waveforms of superimposed 210 spikes detected from the AMP stacked needle electrode (3σ amplitude threshold). For a detailed analysis of these spikes, the amplitude and period from peak to peak of all spikes were plotted two dimensionally in a scatter diagram (*SI Appendix*, Fig. S6*B*), and this indicated that these spikes are unclassified units. In addition, interspike intervals (ISIs, Fig. 4 *E*,

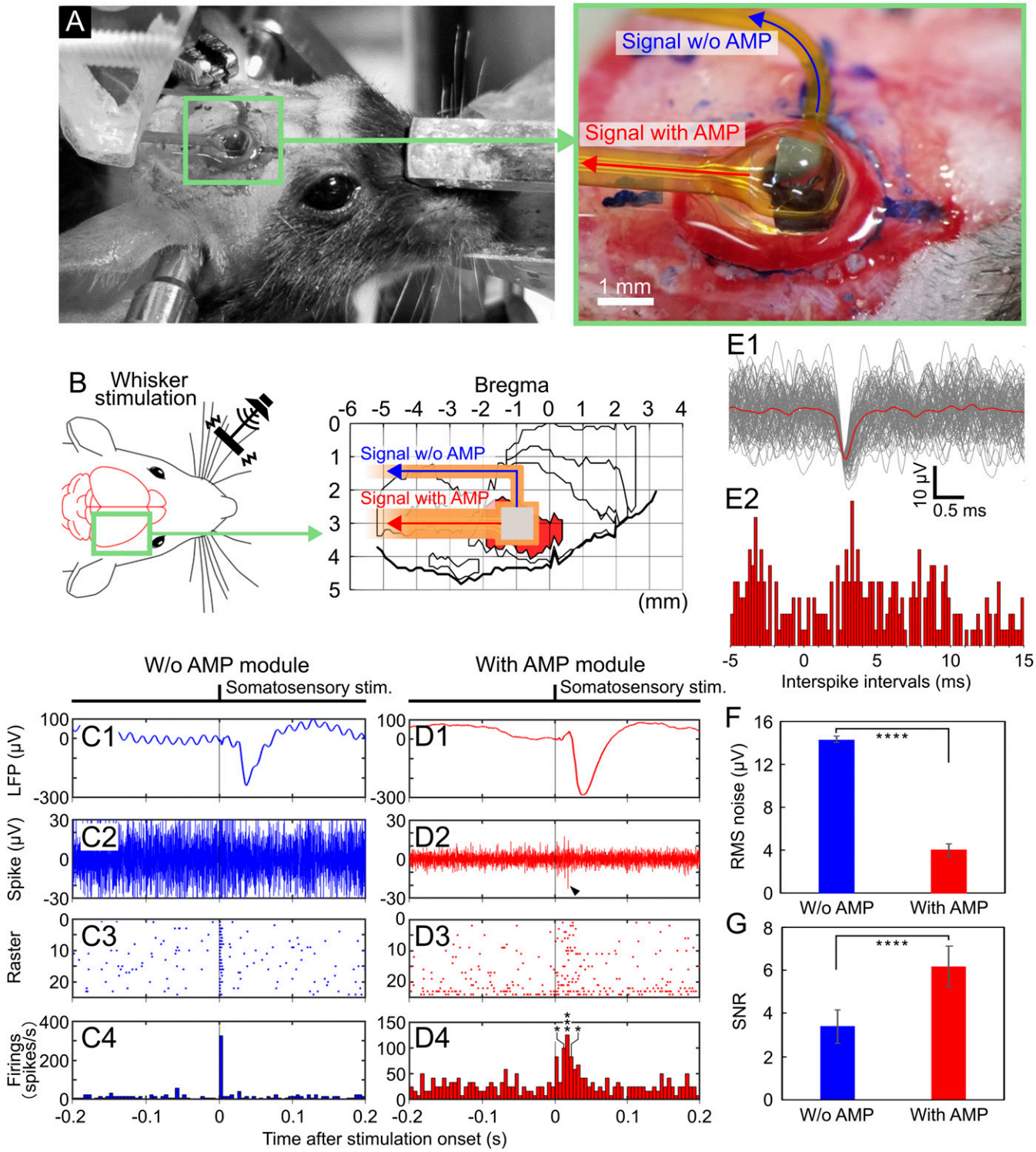

Fig. 4. In vivo neuronal recording via the STACK device. (*A* and *B*) Photographs and schematics representing the device placement position. The device is placed on the barrel field in the primary somatosensory cortex (S1B) of an anesthetized mouse, and the needle electrode penetrates the area of the tissue at a 400-μm needle depth. (*C*, *1*–*4*) Recorded signals via the needle electrode without the AMP module: average waveform of the low-frequency band signals (filtering = 1 to 300 Hz, $n = 24$ trials). (*C*, *1*) High-frequency band-signal waveform from a single trial (filtering = 500 to 3,000 Hz) (*C*, *2*), and raster plot diagrams (*C*, *3*) and PSTHs (*C*, *4*) taken from these signals. (*D*, *1*–*4*) Recorded signals via the needle electrode with the AMP module: average waveform of the low-frequency band signals (filtering = 1 to 300 Hz, $n = 24$ trials) (*D*, *1*), high-frequency band-signal waveform from a single trial (filtering = 500 to 3,000 Hz) (*D*, *2*), and raster plot diagrams (*D*, *3*) and PSTHs (*D*, *4*) taken from these signals. All detection thresholds used were 3× the SD (σ) of the mean signal −0.5 to −1.0 s before stimulus onset. Asterisk denotes a significant spike; $*P < 0.05$, $***P < 0.005$ (*t* test). (*E*, *1*) Enlarged waveforms of superimposed 210 spikes taken from the needle electrode with the AMP module (*D*, *2*–*4*) (3σ-amplitude threshold). (*E*, *2*) ISIs distribution for these spikes. (*F*) rms noise of the needle electrode with the AMP module. The graph also consists of the rms noise without the AMP module for comparison. (*G*) SNRs of the needle electrode with and without the AMP module. Asterisk denotes a significant difference between needle electrodes with and without the AMP module; $****P < 0.001$ (*t* test).

2) for these spikes show a peak amplitude at ∼1 ms. These results suggest that the detected signals did not represent single-unit activity; the detected signal originated from multiple neurons.

Furthermore, we analyzed the effect of attaching the AMP module to the needle electrode on the rms noise and SNR of the high-frequency band signals (filtering = 500 to 3,000 Hz) recorded in vivo. The rms noise with the AMP module was 4.03 ± 0.6 (mean ± SD) μV_{rms}, lower than that without the AMP module [14.3 ± 0.3 (mean ± SD) μV_{rms}] (Fig. 4*F*). The comparison in noise with and without the AMP module yielded a 3.5× higher noise level without the AMP module, suggesting that noise was induced at the device interconnections of the FPC and reduced by the device configuration of the AMP module. The SNR was defined as the peak-to-peak amplitude of the mean waveform 0.005 to 0.055 s after the stimulus onset divided by the rms noise. The SNR with the AMP module yielded 6.18 ± 0.9 (mean ± SD) (15.8 dB), which is more than that without the AMP module [SNR = 3.39 ± 0.8 (mean ± SD) (10.6 dB)] (Fig. 4*G*). We also confirmed the neuronal recording capability of the fabricated STACK device using five other mice. These results indicate that stacking the AMP module (source follower) on the high-impedance microneedle electrode improved the electrical properties of the electrode while enabling the recording of LFP (1 to 300 Hz) and spike signals (500 to 3,000 Hz) from the cortex in vivo.

Wireless Recording. Noise reduction and an increased SNR of the recording system were confirmed in the in vivo recording (Fig. 4), in which the source follower of the AMP module plays a role in the low-output impedance. This circuit configuration enables the high-impedance <3-μm-diameter needle electrode to be connected to numerous signal circuits. For the next step of neuronal recording, the requirements will include wireless recording and the use of an inexpensive and compact data-recording system. To address these requirements, here we demonstrated a circuit configuration of a high-pass filter and a gain stage after the source follower in the STACK device, which was followed by a Bluetooth transmitter for in vivo wireless recording.

We used a commercially available Bluetooth module as the wireless unit (Fig. 5*A* and *SI Appendix*, Text ST3 and Fig. S8). The neuronal signals recorded via the stacked AMP (source follower, −0.175 dB as the front-end amplifier) showed a peak-to-peak amplitude of ∼350 μV for the LFP and ∼50 μV for the spike, in which the signals were further amplified using an externally connected second 40-dB stage amplifier (LT1167, Linear Technology) ("second-stage AMP circuit" in Fig. 5*A* and *SI Appendix*, Fig. S8*B*). The signal out of the second-stage amplifier was followed by the Bluetooth transmitter unit (MM-BTAD4N2, Sanwa Supply Inc.). The amplitude drifts associated with the electrolyte–metal interfacial properties were eliminated before the second-stage amplifier by a high-pass filter with a cutoff frequency of 0.1 Hz (*SI Appendix*, Text ST3 and Fig. S8*B*).

As with the in vivo recording with the "wired" STACK device, we used an anesthetized mouse (male, 30.2 g in weight, 100 μL of 0.5% solution per 10 g body weight for chlorprothixene and 50 μL of 10% solution per 10 g body weight for urethane), whose cranium and dura mater (0 to 2 mm caudal and 2 to 4 mm lateral to the bregma) were removed for needle penetration into the S1B. During the recording, the mouse's whiskers were also stimulated for characterization of the evoked neuronal potentials (*Materials and Methods*).

The wireless recording capabilities of the STACK device were compared with those of the electrode needle without the AMP module, while using the same Bluetooth transmitter. Fig. 5*B* shows the wirelessly recorded signals without the AMP module. LFPs (filtering = 1 to 300 Hz, $n = 150$ trials) from the S1B were repeatedly observed at ∼145 ms because of the delay associated with the wireless Bluetooth unit (*SI Appendix*, Text ST3 and Fig. S8). We generated both the raster plot diagrams and the PSTHs using an amplitude threshold (3σ of the mean signal −0.5 to −1.0 s before the stimulus onset). The artifact caused by the Bluetooth unit (∼120 ms) was confirmed through the recorded data (Fig. 5 *B*, *1*, *3*, and *4*). However, significant high-frequency band signals (filtering = 500 to 3,000 Hz), which responded to the mouse's whisker stimuli, were not observed at ∼145 ms in the recording period. On the other hand, we wirelessly detected both LFP and spike signals via the same needle electrode with the AMP module (STACK device). The low-frequency band-signal waveforms of the LFP (filtering = 1 to 300 Hz, $n = 150$ trials) were repeatedly observed for the 145-ms duration (Fig. 5 *C*, *1*). Fig. 5 *C*, *2* shows the typical high-frequency band-signal waveform (filtering = 500 to 3,000 Hz) taken from the same recording sessions. Fig. 5 *C*, *3* and *4* depicts the raster plot diagrams and PSTHs, respectively, of the spike signals using the same detection threshold (3σ), indicating that spike firings were increased at the same duration of 145 ms. The latency of the neuronal signal recorded with the AMP module was 25 ms, similar to that of signals recorded with the wired STACK device (Fig. 4*D*), when considering a 120-ms duration associated with the wireless signal transmission via Bluetooth. These results indicate that the evoked neuronal signals of the LFP and the spike by the whisker stimuli were wirelessly detected via the STACK device.

Device Implantation. To show the device's capabilities for the chronic recording application, we demonstrated neuronal recording using STACK device–implanted mice. For the recording, the STACK device was implanted at the visual cortex (V1) of the mouse to record visual responses to light stimulation. We used mice ($n = 2$, male, 20.1 to 24.8 g in weight) anesthetized using isoflurane, whose parts of the cranium and dura mater (3 to 5 mm caudal and 1.5 to 3.5 mm lateral to the bregma) were removed to allow for needle penetration at V1. To protect the brain surface, a gelatin sponge was placed over it, and the STACK device was fixed to the skull using dental cement (Fig. 6*A*). A white light-emitting diode (LED) illuminated for 0.5 s at 3-s intervals during the recording session was used for visual stimulation (Fig. 6*B*). The STACK device–implanted mice were healthy, with no death resulting from device implantation.

Fig. 6 *C*, *1* shows the average waveform of low-frequency band signals (filtering = 1 to 300 Hz, $n = 100$ trials) derived from the implanted STACK device in the mouse. Fig. 6 *C*, *2* shows a typical high-frequency band signal (filtering = 500 to 1,000 Hz) in the recording. Fig. 6 *C*, *3* and *4* shows the raster plot diagrams and PSTHs of the spike signals, respectively, detected using the threshold of 3σ of the mean signal −0.5 to −1.0 s before stimulus onset. We confirmed that the firing peak appeared at ∼55 ms, which was consistent with neuronal visual responses recorded using a Pt-black–deposited microelectrode (18) and other devices with flexible electrodes (31), suggesting that these were neuronal responses evoked by visual stimulation.

We examined tissue damage associated with the implanted STACK device (1 × 1 mm^2). Fig. 6*D* shows the histological outcome (coronal brain section) obtained from the V1 of a mouse 2 wk after device implantation, showing the distribution of labeled reactive astrocytes (glial fibrillary acidic protein [GFAP]). The distribution of the astrocytes was compared with the same mouse's brain without the implanted STACK device (right hemisphere with the STACK device and left hemisphere without). Fig. 6*E* shows the quantitative comparison of these astrocytes, indicating no significant difference between them (six slice samples from two mice, *t* test). We also compared the microglia (Iba-1) and cell nuclei (DAPI) (*SI Appendix*, Fig. S9), which showed fewer microglia with the STACK device and no significant difference in cell nuclei. However, these observations suggested that the morphology difference in tissue response was induced by the

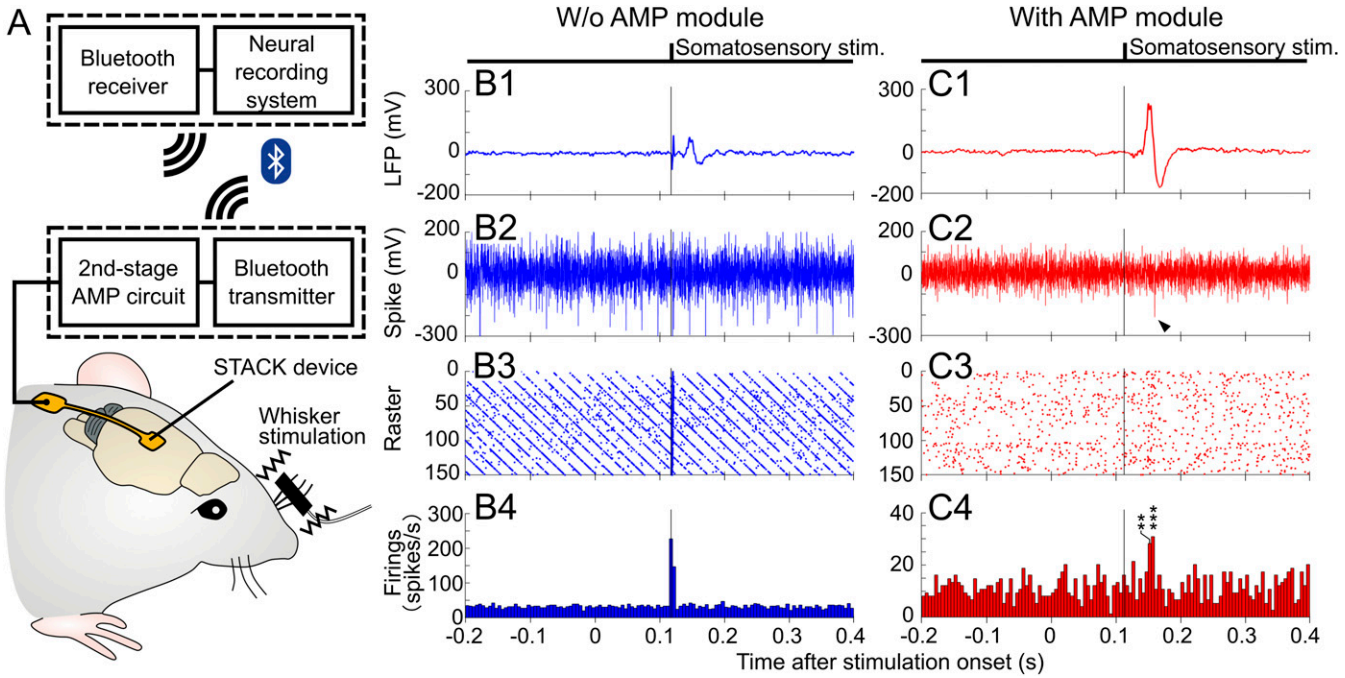

Fig. 5. Wireless in vivo neuronal recording via the STACK device. (*A*) Diagram of the wireless in vivo neuronal recording. The neuronal signals recorded via the STACK device (source follower, −0.175 dB as the front-end amplifier) are further amplified using an externally connected second 40-dB stage amplifier (second-stage AMP circuit, *SI Appendix*, Text ST3 and Fig. S8*B*). The Bluetooth transmitter unit (Bluetooth transmitter) transmits the signal out of the second-stage AMP to a Bluetooth receiver. (*B*, *1*–*4*) Wirelessly recorded signals without the AMP module: average waveform of low-frequency band signals (filtering = 1 to 300 Hz, n = 150) (*B*, *1*), high-frequency band-signal waveform from a single trial (filtering = 500 to 3,000 Hz) (*B*, *2*), and the raster plot diagrams (*B*, *3*) and PSTHs (*B*, *4*) taken from these signals. (*C*, *1*–*4*) Wirelessly recorded signals with the AMP module: average waveform of the low-frequency band signals (filtering = 1 to 300 Hz, n = 150) (*C*, *1*), high-frequency band-signal waveform from a single trial (filtering = 500 to 3,000 Hz) (*C*, *2*), and raster plot diagrams (*C*, *3*) and PSTHs (*C*, *4*) taken from these signals. The detection threshold used for both recordings was 3× the SD (σ) of the mean signal −0.5 to −1.0 s before stimulus onset. Asterisk denotes a significant spike; $^{**}P < 0.01$, $^{***}P < 0.005$ (*t* test).

implanted STACK device. In addition, in both the presence and absence of device implantation, we observed some similar tissue responses which were probably caused by the surgical procedures (e.g., removal of cranium and dura mater). Although these tissue responses must be eliminated for device implantation, the histological data suggest its potential use in chronic applications.

Discussion

We fabricated the NMOS source follower as the AMP module using the Al-interconnection–based in-house 5-μm-gate-length NMOS technology (25). Compared with conventional electrode devices, the STACK device has advantages: 1) device geometry miniaturization, 2) a simplified on-chip MOSFET process, and 3) high device yield. The source follower was designed in a 1 × 1-mm^2 Si substrate consisting of two NMOSs (drive and load transistors, W/L = 50/10 μm for each) and five bonding pads (100 × 100 μm^2 each). The size of each MOSFET can be further miniaturized using state-of-the-art CMOS technology (e.g., the 130-nm CMOS fabrication process), offering an increase in the number of source followers for application to multisite recording within the same device area of 1 × 1 mm^2. For this multichannel-electrode architecture, an electrode module with a small geometric area must be fabricated (e.g., less than 1 × 1 mm^2, depending on the number of source followers) and assembled on the AMP module as an array. Further, the thickness of each module of 525 μm can be reduced by either grinding the module of the Si substrate or using a thin Si substrate in each module process. The thinning processes applied to each Si module will allow us to reduce the device height (electrode module/FPC/AMP module), which will be particularly necessary for device implantation into the animal.

We proposed an assembling technique for an AMP module for a small-needle electrode with high-impedance characteristics. The electrode's impedance might be reduced by either depositing a low-impedance material onto the needle's tip or by increasing the recording area of the electrode. We fabricated a microneedle electrode with a 1-kHz impedance of <500 kΩ by depositing a low-impedance material of Pt black (17, 18). However, the tip area increased to >5 μm in diameter from the original <3 μm. Furthermore, this impedance reduction required the additional process of electroplating Pt black to the needle's tip (21). Another way to reduce the impedance is to increase the recording area by exposing the needle tip (e.g., Pt) from the insulator (e.g., parylene). However, this results in the recording area being increased along with the microneedle, leading to a lack of a localized recording site in the brain tissue. On the other hand, assembling the amplifier close to the microneedle electrode plays an important role in the impedance transformation from the electrode impedance (e.g., >5 MΩ at 1 kHz) to the output impedance of the drive MOSFET (e.g., 7.4 kΩ, *SI Appendix*, Text ST1 and Fig. S1*B*). Moreover, such current buffering of the amplifier helps with noise reduction between the electrode and the data acquisition system, as opposed to without amplifier configuration. This contributes to chronic recording with noise associated with the mouse's electromyography signals and free-moving recording with the cable motion.

The AMP module of the source follower fabricated with our in-house 5-μm-gate-length NMOS technology showed a measured noise level of 15.3 μV rms at 500 to 3,000 Hz. The noise level yielded an SNR of 13.1 dB (signal of a 1-Hz 100-μV sine wave as neuronal activity). The noise level can be further reduced using a p-type MOSFET, together with a large area of the gate. Another method is to use a low-noise transistor, such as a bipolar junction transistor and a junction FET, as well as a buried-channel MOSFET. Although we still need to reduce the noise level

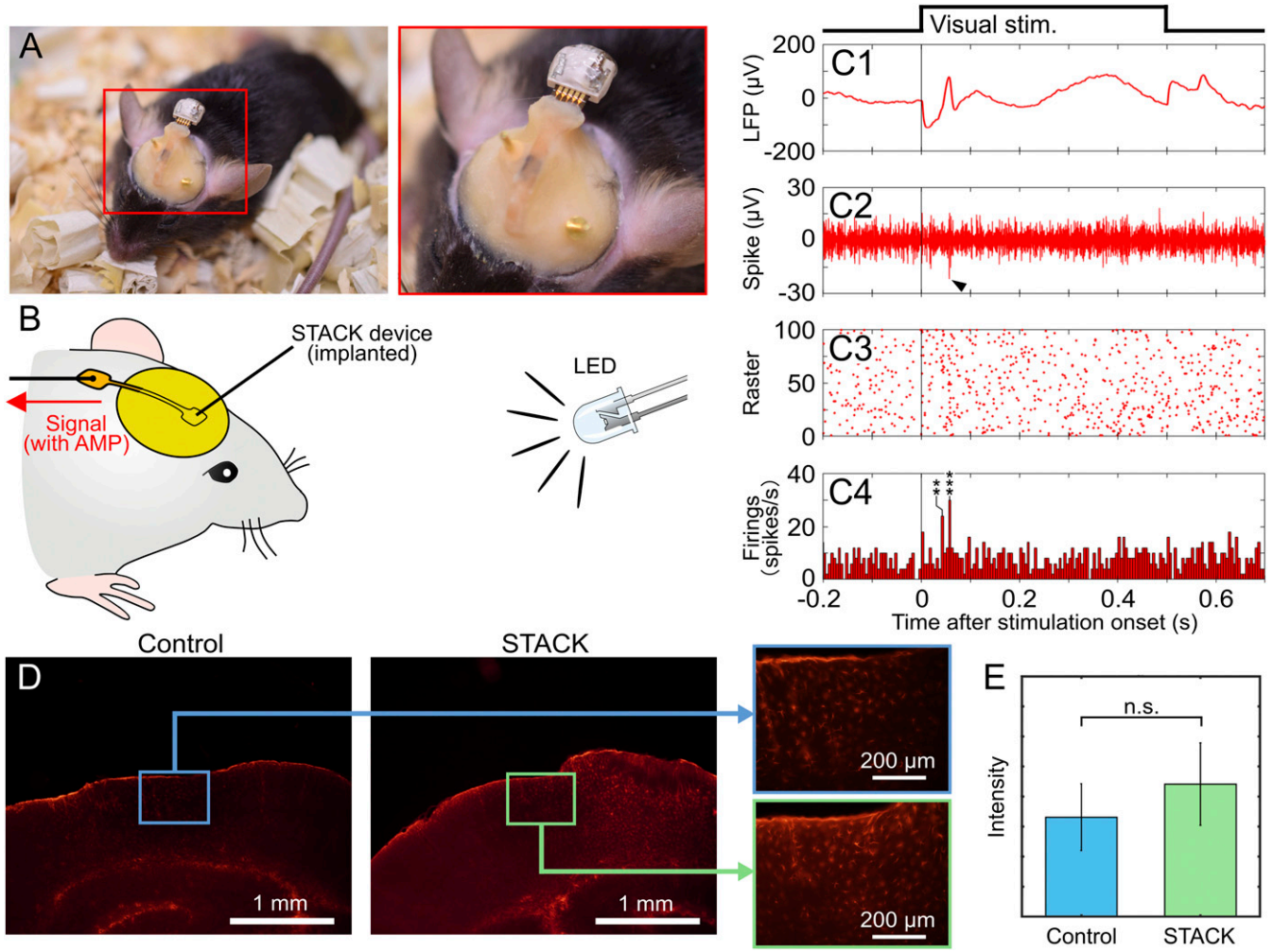

Fig. 6. Device implantation. (*A*) Photographs of a STACK device–implanted mouse. The device is implanted at the visual cortex (V1) of the mouse, and the needle electrode penetrates the area to record the visual responses. (*B*) Schematic representing the recording using an LED for the visual stimulation. (*C*, *1*–*4*) Recorded signals via the implanted STACK device: average waveform of low-frequency band signals (filtering = 1 to 300 Hz, $n = 100$) (*C*, *1*), high-frequency band-signal waveform from a single trial (filtering = 500 to 1,000 Hz) (*C*, *2*), and the raster plot diagrams (*C*, *3*) and PSTHs (*C*, *4*). The detection threshold used was 3× the SD (σ) of the mean signal −0.5 to −1.0 s before stimulus onset. Asterisk denotes a significant spike; $^{**}P < 0.01$, $^{***}P < 0.005$ (*t* test). (*D*) Immunohistochemistry of tissues in a mouse's visual cortex (coronal section) 2 wk after implantation of STACK device (STACK) and without implantation (Control). Tissues were labeled for reactive astrocytes (GFAP). (*E*) Quantitative comparison of the tissues with and without the STACK device using fluorescent intensity in an area of 0.15 mm^2, taken from six slices of samples (*t* test, n.s.: not significant).

in the in vivo neuronal recording, the SNR of the <3-μm-diameter high-impedance electrode of 3.39 (10.6 dB) was improved to 6.18 (15.8 dB) by stacking the fabricated AMP module on the electrode, while the high-frequency band signals of the action potential were detected. Because the AMP module is necessary, however, using the combination of a microneedle with a low-impedance electrode material, such as Pt black (17, 18, 21), iridium oxide (32), PEDOT (22), and hybrid materials [iridium oxide on Pt black (33)], is also an effective method. Additional work will allow us to further miniaturize the diameter of the needle electrode, offering a nanoscale-diameter needle electrode for powerful applications to intracellular recording (28, 34).

The <3-μm-diameter needle electrode was able to record neuronal signals of both the low-frequency band of LFP and the high-frequency band of spikes by stacking the AMP module, although these spike signals originated from multiple neurons (multiunit activity) (Fig. 4 *D* and *E* and *SI Appendix*, Fig. S6*B*). In the whisker stimulation, we used a vibration system, which was connected to several mouse whiskers, to stimulate the whiskers into random directions. Other researchers have used directional deflection of a whisker in order to activate the corresponding neurons in the barrel (35). On the other hand, the vibration system used in this study activated several neurons in the barrel, inducing the recording of multiunit activity. This leads to the necessity of improving the simulation to increase the probability of recording single-unit activity.

By connecting a Bluetooth module to the STACK device, neuronal activities were recorded wirelessly. Although the wireless recording via the STACK device (Fig. 5 *C*, *3* and *4*) showed no significance in the firing rates compared with the wired recording (Fig. 4 *D*, *3* and *4*), we could not detect any high-frequency band signals by wireless recording without the STACK device (Fig. 5 *B*, *3* and *4*). In addition, the low-frequency band signals without the STACK device showed the amplitude attenuations (Fig. 5 *B*, *1*). These signal degradations in both low- and high-frequency band signals are caused by the electrode's high-impedance characteristics, suggesting that the STACK device helps to improve recording quality. To achieve significance in the firing rates of wireless recording, it is essential to reduce the system noise of the wireless recording, including noise components associated with the

Bluetooth module and with the recording cable between the STACK device and the second-stage AMP circuit. We are currently working on facilitating a Bluetooth module-based wireless recording system that reduces these noise components.

A kill zone of less than 10 μm for electrode shafts did not induce major trauma (14), and the damaged area occupied by glial cells is proportional to needle size (cross-sectional area) (11). We also observed damage reduction (less microglia appearance) in our previous work in which immunohistochemical analysis indicated that these Si growth-based 3-μm-diameter needles were less invasive than the larger conventional electrodes (>40-μm diameter) (17). Additional work on our <3-μm-tip-diameter needle electrode is needed to further reduce tissue damage, which is induced by 1) the physical stress associated with the electrode's platform of the Si module (1×1 mm^2 in area, ~1 mm in overall thickness, and ~2.53 mg in weight), 2) the electrode's penetration and the device's placement on the tissue surface, and 3) the device's implantation for the chronic recording application. We examined the tissue responses associated with the implantation of the STACK device for 2 wk. The histological data suggested that the device induced no significant responses from the tissue compared with that caused by the surgical procedures (removal of cranium and dura mater). However, we should further discuss the mechanical mismatch between the hard device (e.g., Si, >130 GPa) and the soft tissue of the brain [on the order of 1 kPa (36, 37)], where the device contacts the surface of brain. Although the mechanical mismatch will induce tissue responses, the surface area of the STACK device of 1×1 mm^2 is smaller than the $>8 \times 3$ mm^2 of our previous needle electrode device (17), enabling the minimization of tissue responses. To further minimize tissue responses, there is a need to make the device's substrate soft and flexible, comparable to brain tissue. This will be fabricated by the Si-growth technology-based device fabrication process, which we are currently developing.

Conclusion

In summary, stacking an AMP module on a <3-μm-diameter high-impedance needle electrode improves the electrical properties of the electrode, exhibiting a sufficiently high SNR to record both the LFP and spike signals from the mouse cortex in vivo. The device geometry was designed to be 1×1 mm^2 to reduce the removal area of the cranium and dura mater of the brain, allowing neuronal recording of a relatively small animal, as demonstrated using mice. In addition to the advantages of the electrical properties and geometry, stacking the AMP module has a higher device yield and promises no degradation of the MOSFET characteristics, compared with the other assemblies of the Si needle electrode on the same substrate of MOSFET by the post-MOSFET process of VLS growth (23–26). Because of the needle diameter of <3 μm and the overall device area of 1×1 mm^2, applications of the fabricated STACK device included low invasive neuronal recording, wireless recording as demonstrated in this work, chronic recording, and multisite recording by placing the devices at multiple brain regions, while providing both LFP and spike signal recording capabilities with a high SNR.

Materials and Methods

Ethics. All experimental procedures were approved by the Committee for the Use of Animals at Toyohashi University of Technology, and all animal care followed the Standards Relation to the Care and Management of Experimental Animals (Notification No. 6, 27 March 1980 of the Prime Minister's Office of Japan).

In Vivo Recording. For somatosensory response recordings, the needle of the electrode module was stereotaxically penetrated into the barrel field in the primary somatosensory cortex (S1B) on the right hemisphere via the fenestra of the cranium and dura mater (0 to 2 mm caudal and 2 to 4 mm lateral to the bregma). The connector end of the STACK device was attached to the manipulator during both needle penetration and device operation. As a signal reference electrode, a stainless-steel screw was drilled into the skull over the cerebellum. Because our device had a single needle electrode with a recording site of <3 μm in diameter, we stimulated several principal whiskers of the mouse to activate the corresponding barrels, eliminating the site mismatch between the recording-site and activated neurons.

After needle-electrode penetration, these whiskers were mechanically stimulated to activate the S1B neurons with an electromagnetic vibrator system (custom built), which was driven by 5-ms-duration pulse signals from the processing system (RZ2, Tucker-Davis Technologies). The stimulus intensity was manually modified to enable observation of the neuronal activity with an interstimulus interval of 3 s. Using the same processing system, timing pulse signals of the stimulations were synchronized to acquire the neuronal signals.

For wired in vivo extracellular recording (Fig. 4), the fabricated STACK devices were connected to a recording amplifier (ZC64, Tucker-Davis Technologies, input impedance = 1×10^{14} Ω) with filters (0.35 Hz for low cutoff and 7.5 kHz for high cutoff). The signals recorded through the amplifier were routed to a preamplifier/digitizer (PZ2, Tucker-Davis Technologies) and acquired with a digital signal-processing module (RZ2, Tucker-Davis Technologies).

Data Availability. All study data are included in the article and/or *SI Appendix*.

ACKNOWLEDGMENTS. We acknowledge support from Japan Society for the Promotion of Science (JSPS) Grants-in-Aid for Scientific Research (KAKENHI) Grants 17H03250, 26709024, and 20H00244 and from the Strategic Advancement of Multi-Purpose Ultra-Human Robot and Artificial Intelligence Technologies Programme from the New Energy and Industrial Technology Development Organization (NEDO). R.N. was supported by the Takeda Science Foundation. K.K. was supported by Toyota Physical & Chemical Research Institute Scholars and JSPS KAKENHI Grant 15H05917.

1. K. Najafi, J. Ji, K. D. Wise, Scaling limitations of silicon multichannel recording probes. *IEEE Trans. Biomed. Eng.* **37**, 1–11 (1990).
2. Q. Bai, K. D. Wise, D. J. Anderson, A high-yield microassembly structure for three-dimensional microelectrode arrays. *IEEE Trans. Biomed. Eng.* **47**, 281–289 (2000).
3. C. Mora Lopez *et al.*, A neural probe with up to 966 electrodes and up to 384 configurable channels in 0.13 μm SOI CMOS. *IEEE Trans. Biomed. Circuits Syst.* **11**, 510–522 (2017).
4. J. J. Jun *et al.*, Fully integrated silicon probes for high-density recording of neural activity. *Nature* **551**, 232–236 (2017).
5. P. J. Rousche, R. A. Normann, A method for pneumatically inserting an array of penetrating electrodes into cortical tissue. *Ann. Biomed. Eng.* **20**, 413–422 (1992).
6. P. J. Rousche, R. A. Normann, Chronic recording capability of the Utah Intracortical Electrode Array in cat sensory cortex. *J. Neurosci. Methods* **82**, 1–15 (1998).
7. L. R. Hochberg *et al.*, Neuronal ensemble control of prosthetic devices by a human with tetraplegia. *Nature* **442**, 164–171 (2006).
8. L. R. Hochberg *et al.*, Reach and grasp by people with tetraplegia using a neurally controlled robotic arm. *Nature* **485**, 372–375 (2012).
9. J. W. Salatino, K. A. Ludwig, T. D. Y. Kozai, E. K. Purcell, Glial responses to implanted electrodes in the brain. *Nat. Biomed. Eng.* **1**, 862–877 (2017).
10. T. Saxena *et al.*, The impact of chronic blood-brain barrier breach on intracortical electrode function. *Biomaterials* **34**, 4703–4713 (2013).
11. D. H. Szarowski *et al.*, Brain responses to micro-machined silicon devices. *Brain Res.* **983**, 23–35 (2003).
12. R. Chen, A. Canales, P. Anikeeva, Neural recording and modulation technologies. *Nat. Rev. Mater.* **2**, 1–16 (2017).
13. V. S. Polikov, P. A. Tresco, W. M. Reichert, Response of brain tissue to chronically implanted neural electrodes. *J. Neurosci. Methods* **148**, 1–18 (2005).
14. D. J. Edell, V. V. Toi, V. M. McNeil, L. D. Clark, Factors influencing the biocompatibility of insertable silicon microshafts in cerebral cortex. *IEEE Trans. Biomed. Eng.* **39**, 635–643 (1992).
15. T. D. Y. Kozai *et al.*, Ultrasmall implantable composite microelectrodes with bioactive surfaces for chronic neural interfaces. *Nat. Mater.* **11**, 1065–1073 (2012).
16. A. Fujishiro, H. Kaneko, T. Kawashima, M. Ishida, T. Kawano, "A penetrating micro-scale diameter probe array for in vivo neuron spike recordings" in *2011 IEEE 24th International Conference on Micro Electro Mechanical Systems* (IEEE, 2011), pp. 1011–1014.
17. A. Fujishiro, H. Kaneko, T. Kawashima, M. Ishida, T. Kawano, In vivo neuronal action potential recordings via three-dimensional microscale needle-electrode arrays. *Sci. Rep.* **4**, 4868 (2014).
18. H. Sawahata *et al.*, Single 5 μm diameter needle electrode block modules for unit recordings in vivo. *Sci. Rep.* **6**, 35806 (2016).
19. S. Yamagiwa *et al.*, "Ultra high-aspect-ratio neuroprobe: 5-μm-diameter and 400-μm-length needle detects action potentials in vivo" in *2017 IEEE 30th International Conference on Micro Electro Mechanical Systems (MEMS)* (IEEE, 2017), pp. 553–556.
20. T. Harimoto *et al.*, Enlarged gold-tipped silicon microprobe arrays and signal compensation for multi-site electroretinogram recordings in the isolated carp retina. *Biosens. Bioelectron.* **26**, 2368–2375 (2011).

21. H. Oka, K. Shimono, R. Ogawa, H. Sugihara, M. Taketani, A new planar multielectrode array for extracellular recording: Application to hippocampal acute slice. *J. Neurosci. Methods* **93**, 61–67 (1999).
22. X. Cui, D. C. Martin, Electrochemical deposition and characterization of poly(3,4-ethylenedioxythiophene) on neural microelectrode arrays. *Sens. Actuators B Chem.* **89**, 92–102 (2003).
23. T. Kawano *et al*., Selective vapor-liquid-solid epitaxial growth of micro-Si probe electrode arrays with on-chip MOSFETs on Si (111) substrates. *IEEE Trans. Electron Dev.* **51**, 415–420 (2004).
24. T. Kawano *et al*., Electrical interfacing between neurons and electronics via vertically integrated sub-4 μm-diameter silicon probe arrays fabricated by vapor-liquid-solid growth. *Biosens. Bioelectron.* **25**, 1809–1815 (2010).
25. A. Okugawa, K. Mayumi, A. Ikedo, M. Ishida, T. Kawano, Heterogeneously integrated vapor–liquid–solid grown silicon probes/(111) and silicon MOSFETs/(100). *IEEE Electron Device Lett.* **32**, 683–685 (2011).
26. H. Makino *et al*., "Vertically aligned extracellular microprobe arrays/(111) integrated with (100)-silicon MOSFET amplifiers" in *2015 28th IEEE International Conference on Micro Electro Mechanical Systems (MEMS)* (IEEE, 2015), pp. 686–689.
27. A. Ikedo, T. Kawashima, T. Kawano, M. Ishida, Vertically aligned silicon microwire arrays of various lengths by repeated selective vapor-liquid-solid growth of n-type silicon/n-type silicon. *Appl. Phys. Lett.* **95**, 033502 (2009).
28. Y. Kubota *et al*., Nanoscale-tipped high-aspect-ratio vertical microneedle electrodes for intracellular recordings. *Small* **12**, 2846–2853 (2016).
29. G. Buzsaki, Neuronal oscillations in cortical networks. *Science* **304**, 1926–1929 (2004).
30. G. Buzsáki, C. A. Anastassiou, C. Koch, The origin of extracellular fields and currents–EEG, ECoG, LFP and spikes. *Nat. Rev. Neurosci.* **13**, 407–420 (2012).
31. K. Yamashita *et al*., Flexible parylene-thread bioprobe and the sewing method for in vivo neuronal recordings. *Sens. Actuators B Chem.* **316**, 127835 (2020).
32. S. F. Cogan, Neural stimulation and recording electrodes. *Annu. Rev. Biomed. Eng.* **10**, 275–309 (2008).
33. S. Yamagiwa *et al*., Layer-by-layer assembled nanorough iridium-oxide/platinum-black for low-voltage microscale electrode neurostimulation. *Sens. Actuators B Chem.* **206**, 205–211 (2015).
34. Y. Kubota *et al*., Long nanoneedle-electrode devices for extracellular and intracellular recording in vivo. *Sens. Actuators B Chem.* **258**, 1287–1294 (2018).
35. M. L. Andermann, C. I. Moore, A somatotopic map of vibrissa motion direction within a barrel column. *Nat. Neurosci.* **9**, 543–551 (2006).
36. S. Budday *et al*., Mechanical properties of gray and white matter brain tissue by indentation. *J. Mech. Behav. Biomed. Mater.* **46**, 318–330 (2015).
37. G. Hong, C. M. Lieber, Novel electrode technologies for neural recordings. *Nat. Rev. Neurosci.* **20**, 330–345 (2019).